Synthesis and supramolecular organization of the iodide and triiodides of a polycyclic adamantane-based diammonium cation: the effects of hydrogen bonds and weak I⋯I interactions†

Ivan A. Mezentsev-Cherkes,[a] Tatiana A. Shestimerova,[a] Aleksei V. Medved'ko,[b] Mikhail A. Kalinin,[a] Alexey N. Kuznetsov, [iD][ac] Zheng Wei,[d] Evgeny V. Dikarev, [iD][d] Sergey Z. Vatsadze [iD] *[ab] and Andrei V. Shevelkov [iD] *[a]

A careful selection of organic and inorganic components enables the production of unusual structure types with promising practical properties by facile syntheses. In this paper, we describe novel supramolecular architectures comprising organic adamantane-like divalent building blocks and iodide or polyiodide anions. Highly acidic conditions facilitated the formation of a doubly protonated organic ligand out of 5,7-dimethyl-1,3-diazaadamantane that generates three different crystal structures with inorganic counterions. In these structures, cationic substructures are constructed by transforming neutral organic ligands into $[(C_{10}N_2H_{20})I]^+$ or $[(C_{10}N_2H_{20})(H_2O)]^{2+}$ cations, which crystallize with charge-compensating iodine-based anions of different complexities. All three crystal structures are characterized by various noncovalent forces, ranging from strong (N)H⋯I, (O)H⋯I, and (N)H⋯O hydrogen bonds to secondary and weak I⋯I interactions. Raman and diffuse reflectance spectroscopy as well as DFT calculations were employed to describe the electronic structures and optical properties of new supramolecular architectures, with particular attention to the role of non-covalent interactions.

Introduction

Polyiodides have been known for many decades. They have attracted the interest of many researchers because of their fascinating crystal structures and a variety of applications from the century-old analytical use of iodine–starch blue to conducting polymers and Grätzel solar cells.[1–3] The recent reemergence of interest in polyiodides has been evoked in the wake of the discovery of a new synthetic route to the so-called perovskite solar cells. This technique involves polyiodides as reaction media to convert metallic lead into light-harvesting materials.[4–6] In view of this approach, not only has the exploratory synthesis of polyiodides become the topic of investigations, but other directions have also emerged, including an analysis of the weak bonding that governs the reactivity of polyiodides. Along these lines, the investigations of supramolecular architectures involving polyiodide anions are becoming more visible, as they provide information on how a combination of multifold weak bonds may influence the overall stability of a compound and, hence, its reactivity.[7,8]

Triiodides are by far the most abundant family within the diverse class of polyiodides. Depending on the details of a particular crystal structure, they vary in geometry, being more or less symmetric, and share a common structural property, namely, an average interatomic I–I distance that spans a very narrow window of 2.91–2.94 Å.[9–11] At the same time, the involvement of triiodides in a crystal structure largely depends on their interactions with charge-balancing cations. In the case of simple inorganic cations such as K⁺, the electrostatic forces dominate. For complex cations, other forces ensure the bonding between them and triiodide anions; these include the hydrogen H⋯I bonds, I⋯I interactions of various strengths, and even weak contacts between iodine and other electronegative elements, such as S⋯I.[11–23]

[a] Department of Chemistry, Lomonosov Moscow State University, 119991 Moscow, Russia. E-mail: szv@org.chem.msu.ru, shev@inorg.chem.msu.ru

[b] N.D. Zelinsky Institute of Organic Chemistry RAS, 119991 Moscow, Russia

[c] N. S. Kurnakov Institute of General and Inorganic Chemistry RAS, 119991 Moscow, Russia

[d] Department of Chemistry, University at Albany, SUNY, Albany, New York 12222, USA
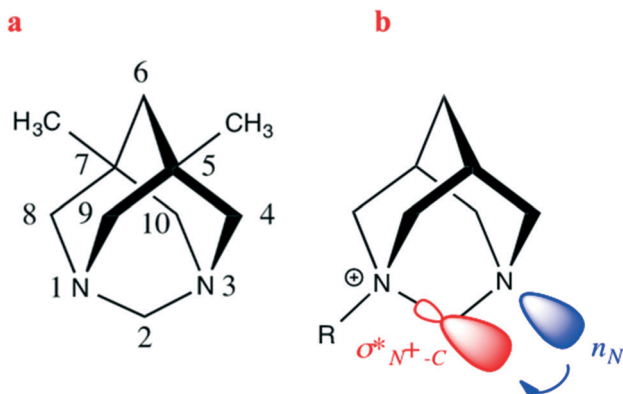
Fig. 1 General view of 1,5-dimethyl-1,3-diazaadmantane with atom numbering (a); illustration of the anomeric effect in 1-alkylated/protonated DAD (b).

1,3-Diazaadamantanes (DADs, Fig. 1) represent derivatives of the parent hydrocarbon adamantane, in which two nitrogen atoms occupy the bridgehead positions of the tricyclic core in such a manner that they can affect each other due to orbital effects. Indeed, the examination of the CSD database (ESI,† Table S1) clearly shows that whilst neutral DAD molecules feature more or less equal $R_2N–CH_2$ distances (1.470–1.475 Å), in monoprotonated and monoalkylated species, these distances significantly differ (1.399–1.430 Å for $R_2N–CH_2$ and 1.521–1.556 Å for $R_3 + N–CH_2$). These data represent a clear manifestation of the anomeric effect when a nitrogen lone pair effectively donates electron density to the σ*-orbital of the adjacent $CH_2–N + R_3$ bond, inducing appropriate changes in N–C–N distances (Fig. 1b). The only reasonable structure of dicationic DAD contains dimethylated dications with R_3+N-CH_2 distances equal to 1.464 and 1.519 Å; however, the cation itself is asymmetric because the OH group on one of the carbon atoms is *syn* with respect to one nitrogen atom and *anti* to the other (Table S1 of ESI,† for details).

An analysis of the crystal structures of DADs reported in the literature suggests the angular nature of this dinitrogen building block; indeed, the "bite angle" between the directions of the nitrogen lone pairs lies in the range of 105–106 degrees (Table S1 of ESI†). While DADs in the form of a free base could be regarded as angular di-donor supramolecular tectons (containing two hydrogen bond acceptors), in the diprotonated form, they should represent angular di-acceptor tectons (containing two hydrogen bond donors).

To the best of our knowledge, no attempts have been made to explore the DAD building block in the construction of extended supramolecular architectures using one or both nitrogens as electron density centers and the whole adamantane-like molecule as an angular-type linker. Di-protonated DADs have also not yet been documented.

In this work, 5,7-dimethyl-1,3-diazaadamantane ($C_{10}N_2H_{18}$, Fig. 1a) was chosen to provide a template effect in assembling new compounds with various inorganic anions

made purely of iodine atoms. We present three new compounds; two of them feature a complex $[(C_{10}N_2H_{20})I]^+$ cation with a chain-like structure that slightly changes to accommodate anions of different complexities, a standalone I^- or a triiodide I_3^-, whereas the third compound features an intricate array of loosely bound I_3^- anions interacting with $[(C_{10}N_2H_{20})(H_2O)]^{2+}$ cations. Special attention is brought to hydrogen bonds that are different in strength within the complex cation and between the cations and anions as well as to interanionic $I_3^-\cdots I_3^-$ interactions.

Results and discussion

Compounds $[(C_{10}N_2H_{20})I]I$ (**1**), $[(C_{10}N_2H_{20})I]I_3$ (**2**), and $[(C_{10}N_2H_{20})(H_2O)](I_3)_2$ (**3**) were prepared by dissolving 5,7-dimethyl-1,3-diazaadamantane, $C_{10}N_2H_{18}$, in hydroiodic acid with a stoichiometric amount of iodine. Compound **1** forms a yellowish-white polycrystalline solid, whereas **2** and **3** are obtained as needle-like brown and grey crystals, respectively. The purity of all three compounds was confirmed by comparing the experimental XRD patterns with those calculated from the crystal data (see Fig. S1–S3 of the ESI†). The compounds are stable at room temperature but start to decompose upon heating at 163 °C (**1**), 98 °C (**2**), and 79 °C (**3**) (see Fig. S4–S6 of the ESI†).

Compounds **1** and **2** crystallize in different crystal structures with dissimilar unit cell volumes of 2858 and 901 $Å^3$, respectively (Fig. 2); however, they show some common structural features. In both structures, the organic part appears as a doubly protonated cation $C_{10}N_2H_{20}^{2+}$ linked by I^- anions into cationic chains $[(C_{10}N_2H_{20})I]^+$. The anionic parts differ in the structures of **1** and **2**. In **1**, monoatomic I^- anions compensate the charge of a one-dimensional cation, whereas in the structure of **2**, the triiodide anions I_3^- serve as counterions.

The $C_{10}N_2H_{18}$ diazaadamantane is doubly protonated due to the action of strong hydroiodic acid. In both crystal
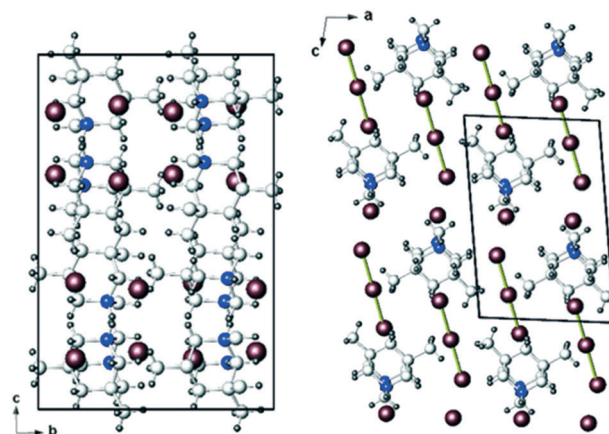

Fig. 2 Views of the crystal structure of **1** along the *a* axis (left) and of **2** along the *b* axis (right). Iodine, brown; nitrogen, blue; carbon, light grey; hydrogen, dark grey.

structures, it transforms into the $(C_{10}N_2H_{20})^{2+}$ cation, which exploits hydrogen atoms on both nitrogens to form rather short hydrogen bonds with I⁻. The (N)H···I distances range from 2.40 to 2.42 Å in **1** and from 2.50 to 2.57 Å in **2**. The former distances point to strong hydrogen bonding, which is rarely found in such systems. The latter distances also confirm the strength of the hydrogen bonds. Although similar (N)H···I contacts can be found in the literature,[24] they are still considerably shorter than the typical (N)H···I bond lengths of 2.70–2.90 Å.[25–27] As a consequence of hydrogen bonding, the cationic $[(C_{10}N_2H_{20})I]^+$ chains are formed (Fig. 3). The chains are slightly dissimilar in **1** and **2** not only because the (N)H···I bonds have a different length, but also because the H···I···H angles are 106 and 115 degrees in **1** and **2**, respectively, whereas the N–H···I angles are 159–170 degrees. Although the chains are zigzagged and run parallel to each other in both structures, they demonstrate different curvatures and thus create voids of different volumes to be filled by charge-balancing anions, namely I⁻ in **1** and I_3^- in **2** (Fig. 3).
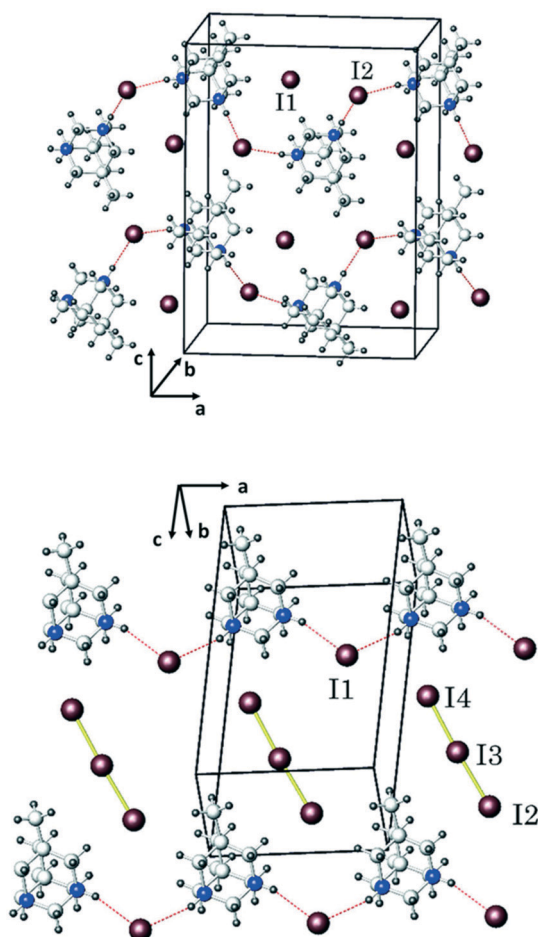
The crystal structure of **3** is more complex despite the fact that it contains the same doubly protonated 5,7-dimethyl-1,3-diazaadamantane cation, which coexists with triiodide anions and water molecules (Fig. 4).

In the structure of **3**, each $(C_{10}N_2H_{20})^{2+}$ cation uses its two NH_2 groups to form two hydrogen bonds, one with water oxygen and the other with iodine of the I_3^- anion. In turn, each water molecule uses both hydrogen atoms to form hydrogen bonds with I_3^- anions. In this way, each water oxygen and each nitrogen adopt a coordination number of three and four, respectively (Fig. 5). However, the strongest hydrogen bonding is formed between the diazaadamantane cation and water; the (N)H···O bonds of 1.78 Å are shorter than typical bonds of this kind, which have lengths of 1.8–1.9 Å. In contrast, the (N)H···I distances are quite long, ranging from 2.84 to 2.96 Å, which is significantly longer than those in **1** and **2** (Table 1). The (O)H···I hydrogen bonds are also relatively long and cover the range of 2.72–2.98 Å.

Therefore, the crystal structure of **3** can be viewed as consisting of the $[(C_{10}N_2H_{20})(H_2O)]^{2+}$ cations and twice as many I_3^- anions, yielding the charge-balanced composition $[(C_{10}N_2H_{20})(H_2O)](I_3)_2$.

The doubly protonated diazaadamantane $(C_{10}N_2H_{20})^{2+}$ cation exhibits a symmetric N–CH$_2$–N bridge in all three crystal structures. Within the bridge, the N–C distances are 1.46–1.49 Å in the crystal structures of **1** and **3** but are only slightly shorter, namely 1.45 and 1.49 Å, in **2**. For comparison, in the monoprotonated diazaadamantane $(C_{10}N_2H_{19})^+$ cation, the N–CH$_2$–N bridge is highly unsymmetric; the distance from carbon to the protonated nitrogen atom is 1.54 Å, whereas the distance to the nitrogen baring a lone pair is only 1.42 Å.[28] We note that such asymmetry is typical for monoprotonated derivatives of the adamantane family, and it is due to the anomeric effect mentioned above. For instance, in the crystal structure of urotropinium triiodide, the lengths of the C–N bonds to the protonated and neutral nitrogen atoms differ by nearly 0.1 Å.[29] The N–C–N angles in all three crystal structures are nearly the same; they fall in a short range of 107–109 degrees.

Fig. 3 Zigzag cationic $[(C_{10}N_2H_{20})I]^+$ chains and guest anions in the crystal structures of **1** (top) and **2** (bottom). Iodine, brown; nitrogen, blue; carbon, light grey; hydrogen, dark grey. Hydrogen (N)H···I bonds are shown by dashed red lines.
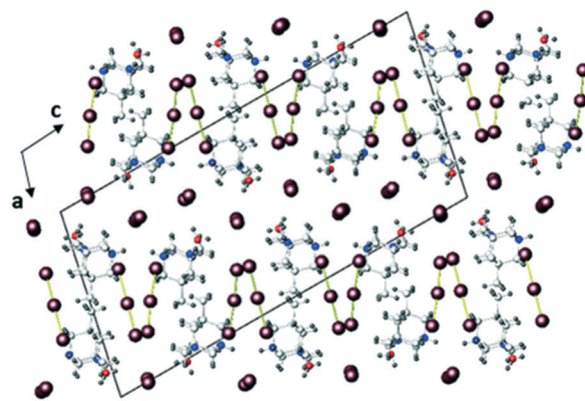

Fig. 4 Projection of the crystal structure of **3** onto the (ac) plane. Iodine, brown; nitrogen, blue; carbon, light grey; hydrogen, dark grey.
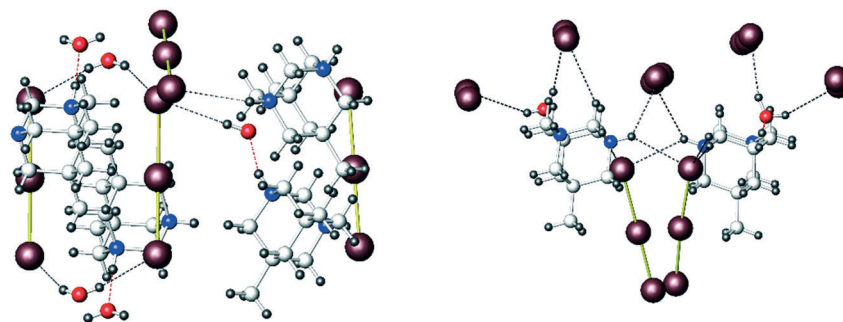
Fig. 5 Fragments of the crystal structure of **3** viewed along the *a* (left) and *b* (right) axes. Iodine, brown; nitrogen, blue; oxygen, red; carbon, light grey; hydrogen, dark grey. Hydrogen (O)H⋯I and (N)H⋯I bonds are shown by dashed black lines, and (N)H⋯O bonds are shown by dashed red lines.

At the same time, the N⋯N distances within the $(C_{10}N_2H_{20})^{2+}$ cation are 2.39 Å in **1**, 2.37 Å in **2**, and 2.40–2.41 Å in **3**. These are noticeably shorter than those in the neutral 5,7-dimethyl-1,3-diazaadamantane, where they range from 2.44 to 2.49 Å.[30]

All three crystal structures show no sign of disorder, including positioning of the anions in the voids left by the $[(C_{10}N_2H_{20})I]^+$ zigzag cationic chains in **1** and **2** or the $[(C_{10}N_2H_{20})(H_2O)]^{2+}$ cations in **3**. The proper positioning of the anions is ensured by a number of weak (C)H⋯I hydrogen bonds. The (C)H⋯I distances are significantly longer than the (N)H⋯I ones and cover the range of 2.86–3.14 Å in the structure of **1**, 2.98–3.18 Å in **2**, and 3.02–3.35 Å in **3**; all these distances are typical for these kinds of hydrogen bonds.[25,31,32] In total, there are eight (C)H⋯I hydrogen bonds per anion in the crystal structures of **1** and **2** (ESI,† Fig. S7) and from seven to eleven for four crystallographically independent I_3^- anions in **3**. The length of these hydrogen bonds points at much weaker interactions between the

cations and anions in the three crystal structures compared to the (N)H⋯I bonds within the cationic chains. At the same time, even the longest distance of 3.35 Å is considerably shorter than the sum of the respective van der Waals radii, which can be estimated as 3.7–3.9 Å according to different sources.[33,34]

The geometry of I_3^- anion is only slightly affected by the weak hydrogen bonds in **2**. The I–I distances are 2.90 and 2.91 Å, and the I–I–I angle is 177.6 deg. In contrast, the I–I distances in **3** cover a broad range of 2.82–3.06 Å, being different in four crystallographically independent I_3^- units (Table 2). However, in all I_3^- anions in both crystal structures, the average I–I distance falls within the range of 2.91–2.94 Å, which is typical for these anions regardless of their actual symmetry.[9–11] In accord with these findings, the Raman spectra of **2** and **3** (Fig. 6) are almost identical and typical for asymmetric I_3^- anions;[35] they feature a strong signal at 115 cm^{-1} with an overtone near 230 cm^{-1}, which can be ascribed to the symmetric stretching of the anion. The latter is observed at 110–118 cm^{-1} depending on the average I–I distance.[1,36,37] A weaker peak at 152 (**2**) or 161 (**3**) cm^{-1} can be attributed to the asymmetrical stretching of I_3^-, which is

Table 1 Hydrogen bonding in the crystal structures of **1–3**

D–H⋯A	d(H⋯A), Å	d(D⋯A), Å	Angle (D–H⋯A),°
$[(C_{10}N_2H_{20})I]I$ (**1**)			
N1–H1⋯I2^a	2.40	3.386(2)	170
N2–H2⋯I2^b	2.42	3.389(2)	162
C4–H4B⋯I1	2.86	3.810(2)	161
$[(C_{10}N_2H_{20})I]I_3$ (**2**)			
N1–H1⋯I1	2.50	3.445(16)	161
N2–H2⋯I1^c	2.57	3.498(17)	159
C1–H1A⋯I3^d	2.98	3.92(3)	162
$[(C_{10}N_2H_{20})(H_2O)](I_3)_2$ (**3**)			
O1–H1C⋯I2^e	2.98(9)	3.715(7)	153(11)
O1–H1D⋯I4	2.90(9)	3.729(7)	160(10)
O2–H2C⋯I5^f	2.72(9)	3.567(8)	157(11)
O2–H2D⋯I4	2.74(10)	3.588(8)	153(11)
N1–H1⋯I8^f	2.91	3.618(8)	128
N1–H1⋯I10^g	2.84	3.633(8)	137
N3–H3⋯I5^f	2.86	3.629(8)	134
N3–H⋯I9^g	2.96	3.715(7)	133
N4–H4⋯O2^h	1.69	2.645(12)	159
N2–H2⋯O1	1.78(12)	2.678(10)	175(11)

Symmetry codes: (a) −*x* + 1/2, −*y* + 2, *z* − 1/2; (b) −*x*, −*y* + 2, −*z* + 1; (c) *x* − 1, *y*, *z*; (d) *x*, *y*, *z* − 1; (e) −*x*, −*y*, −*z*; (f) −*x*, −*y* + 1, −*z*; (g) *x* + 1, *y* + 1, *z*; (h) −*x* + 1/2, *y* + 1/2, −*z* + 1/2.

Table 2 Selected interatomic distances and angles in the anionic parts of the crystal structures of **2** and **3**

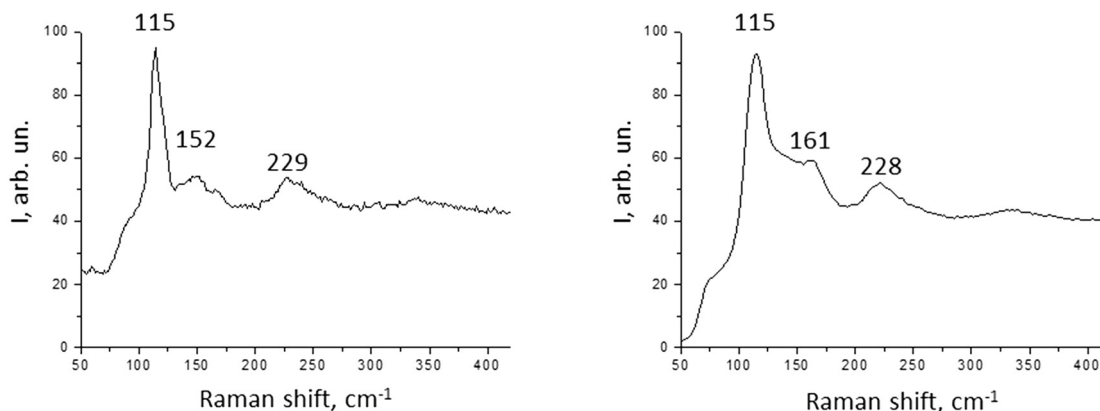| Atoms		Distance, Å	Atoms	Angle,°
$[(C_{10}N_2H_{20})I]I_3$ (**2**)				
I2	– I4	2.897(3)	I4–I2–I3	177.59(10)
	– I3	2.905(3)		
$[(C_{10}N_2H_{20})(H_2O)](I_3)_2$ (**3**)				
I1	– I2	2.9026(9)	I2–I1–I4	176.37(3)
	– I4	2.9435(9)		
I3	– I5	2.9294(9)	I8–I3–I5	177.67(3)
	– I8	2.9169(10)		
I6	– I10	3.0325(10)	I12–I6–I10	175.34(3)
	– I12	2.8480(10)		
I11	– I7	2.8208(10)	I7–I11–I9	179.68(3)
	– I9	3.0628(10)		
O1	– H1C	0.80(8)	H1C–O1–H1D	119(10)
	– H1D	0.87(8)		
O2	– H2C	0.91(8)	H2C–O2–H2D	114(10)
	– H2D	0.93(8)		

Fig. 6 Raman spectra of compounds **2** (left) and **3** (right).

forbidden for D_{ih} symmetry but can be observed if the actual symmetry of the anion is lower.[38,39] A shoulder slightly below 90 cm^{-1}, which is difficult to see for **2** but more pronounced for **3**, is difficult to attribute because this region of the Raman shifts may reveal doubly degenerate bending vibrations of asymmetric I_3^- anions (forbidden by selection rules for the D_{ih} point group) and the stretching vibrations of strong hydrogen bonds.

In the crystal structure of **2**, the I_3^- anions are further distant from each other. In contrast, the crystal structure of **3** features a complex arrangement of I_3^- anions in which they build a strand running along the b axis of the unit cell (Fig. 7). The strand exhibits several modes of the I_3^- anions assembling with different interanionic distances. Within the anionic strand, the shortest contacts of 3.57 and 3.59 Å are observed between the anions running along the b direction in a head-to-tail fashion. Those distances are considerably longer than is typical for bonds within I_3^- anions but are much shorter than the van der Waals contacts. Such interatomic distances are frequently observed in various polyiodides, where I_3^- fragments are stacked to form one- or two-dimensional arrays. Indeed, in many triiodides, the head-to-tail $I_3^-\cdots I_3^-$ contacts vary in a wide range of interatomic distances, from relatively short (near 3.2 Å) to

rather long, approaching 4 Å.[40,41] Remarkably, the I$\cdots$I distances of 3.57 and 3.59 Å can be compared with the intermolecular $I_2\cdots I_2$ distances in crystalline diiodine, 3.50 Å, which ensure properties of this solid such as metallic luster and semiconducting behavior.[2] Generally, the interatomic I$\cdots$I distances that are longer than in the I_3^- anion but shorter than in the van der Waals contacts are called the secondary bonds.[40]

Other interactions within the strand are more distant, from 3.91 to 4.24 Å; they are indicative of much weaker $I_3^-\cdots I_3^-$ interactions and can be compared with the I$\cdots$I van der Walls contacts, which amount to 3.9–4.3 Å according to different literature sources.[42]

More insight into the contribution of iodine units to the behavior of the compound, and, in particular, the role of interanionic $I_3^-\cdots I_3^-$ contacts in the assembling of the crystal structure of **3** can be obtained from the quantum chemical calculations data.

The calculated total and projected densities of states near the Fermi level are shown in Fig. 8. As can be seen from the plots, the compound is a semiconductor with a band gap of *ca.* 1.25 eV. The top of the valence band, as well as the bottom of the conduction band, consist exclusively of contributions from the iodine 5*p* electrons. Notably, while
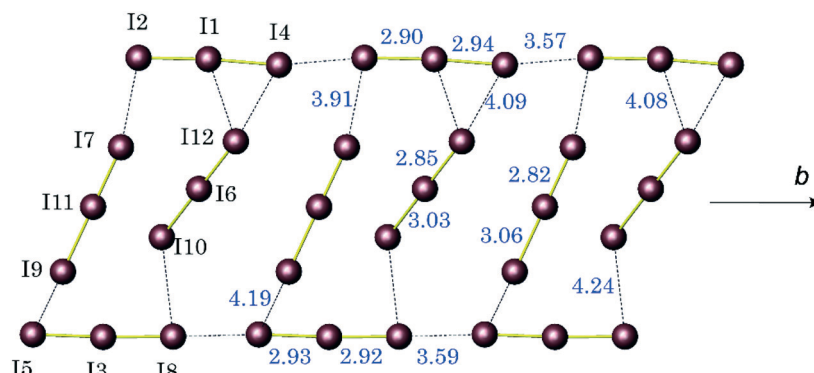

Fig. 7 Fragment of a strand composed of I_3–anions running along the b axis in the crystal structure of **3**. Selected interatomic distances are shown in Å.
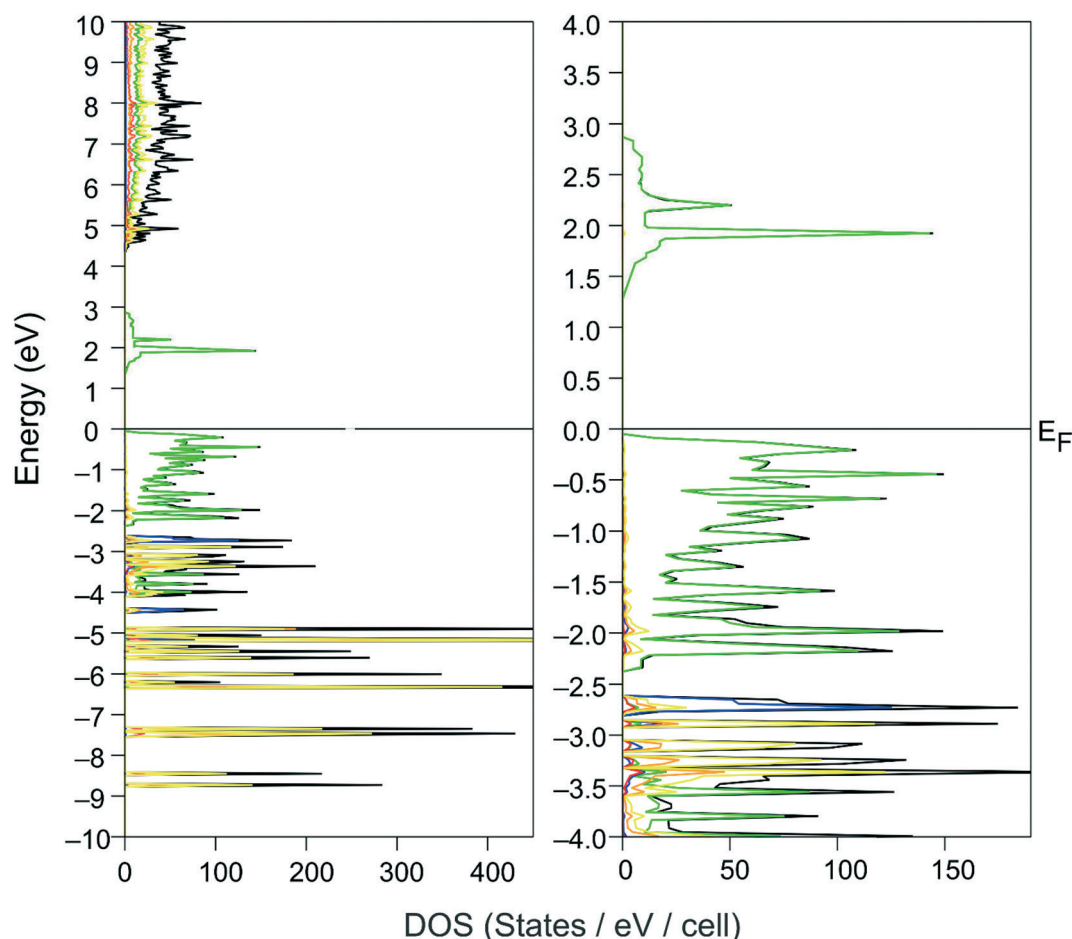
Fig. 8 Total (TDOS) and projected (PDOS) densities of states near the Fermi level for **3** (full-scale and enlarged): TDOS – black, I PDOS – green, O PDOS – blue, N PDOS – orange, C PDOS – red, H PDOS – yellow.

the *p*-states of O, C, and N and the *s*-states of H are mixed to a large extent, there is little to no mixing of the iodine *p*-states with other states from the Fermi level down to *ca.* −2.5 eV. This implies that no covalent interactions occur between the iodine units and the other parts of the structure.

Fig. 9 shows that the compound **3** is a direct-gap semiconductor; the gap is at the X point. The band dispersion is rather anisotropic in this structure, with Γ–Y and D–Z directions in the Brillouin zone showing almost flat bands (*i.e.* very low mobility of charge carriers) and Γ–X and X–Z showing steep band slopes. This can be attributed to the mobility of the charge carriers in this structure being mostly in the *ab* plane, particularly in the *b*-direction.

Chemical bonding in the iodine sublattice was investigated by analyzing the electron localization indicator (ELI-D) topology (Fig. 10).

The ELI-D plots confirm that the iodine network is built of I_3^- units, which are slightly asymmetric and show one covalent I–I bond (Ω1, see Fig. 10), and a third iodine atom at a slightly longer distance carrying a slightly larger charge, which shows no ELI-D attractor between this third iodine atom and the I–I unit. The distances within the I_3^- units vary from almost equal to differing by up to *ca.* 0.2 Å. This is quite typical for I_3^- anions

and is in general agreement with the description provided in the literature.[43] As ELI-D shows no indications of covalency between different I_3^- anions, weaker interactions must be analyzed in order to reveal the nature of the intermolecular forces between iodine units. A useful tool to visually analyze weak interactions is the so-called non-covalent interaction (NCI) analysis based on the reduced density gradient (RDG) method.[44,45] Using this method, one can observe the regions with relatively strong attraction and weak interaction regions, which are differentiated by the electron density values ($\rho(r)$); small values correspond to weak interactions (van der Waals, dispersive, *etc.*), and intermediate-to-strong values correspond to NCI – hydrogen bonds, halogen bonds, *etc.*

Fig. 11 shows that the intramolecular and intermolecular interactions in the I_3^- units have different natures. Within the I_3^- fragments, we observed a combination of covalent and halogen bonding (blue discs), which was characterized by relatively strong attractive forces and medium electron density. The other regions, colored in green, correspond to weak attractive forces and near-zero electron densities, *i.e.* weak NCI. Based on the RDG values, the strongest of these NCIs are the I2–I4 interactions, which provide linking of the I_3^- anions into chains along the *b*-direction. Weaker NCI links of I12–I6–I10 and I4–
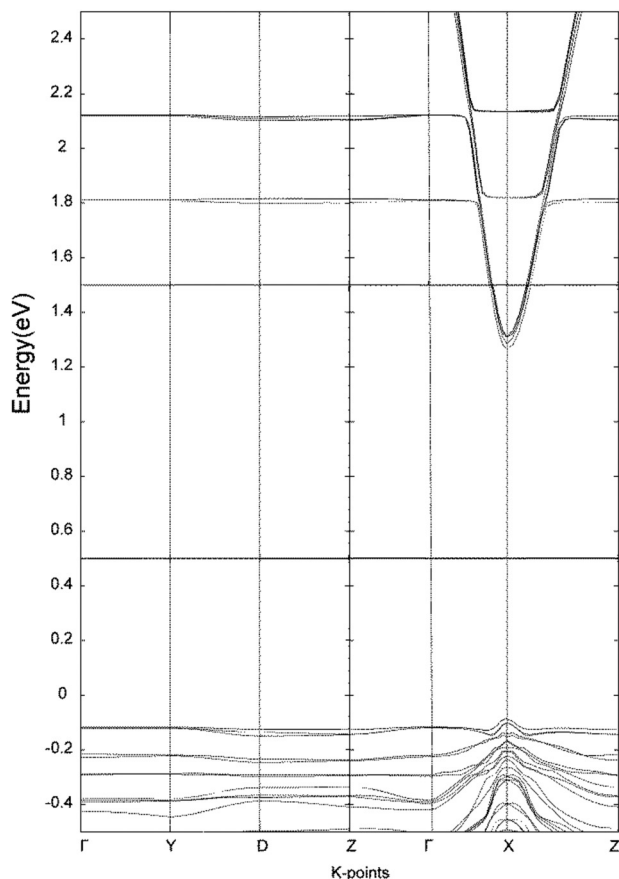
Fig. 9 Calculated band structure near the Fermi level for compound **3**. The coordinates of the special points are Γ (0;0;0), Y (0;0;0.5), D (0.5;0;0.5), Z (0.5;0;0), X (0;0.5;0).
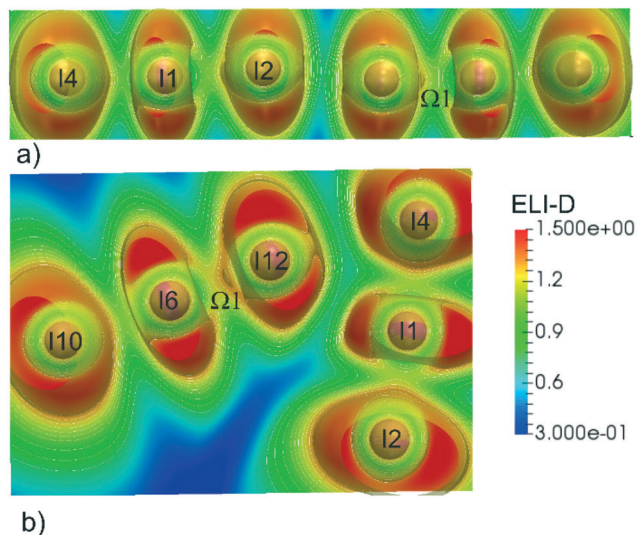

Fig. 10 ELI-D sections and iso-surfaces (Y = 1.22, golden) for two modes of iodine linkage: I4–I1–I2 chains (a), and two I_3^- units at an angle (b).

Fig. 11 NCI plots for various groupings of the I_3^- units in the structure of **3** – I_3–I_3 chain (a), I_3–I_3 angle (b), I_3–I_3–I_3 group (c): blue disks represent strong interactions (halogen bonds, around bond areas), and green disks represent weak interactions (van der Waals and dispersive).

I1–I2 units through van der Waals interactions between I12–I4 and I12–I1 were observed (see Fig. 11b). Moreover, the weakest

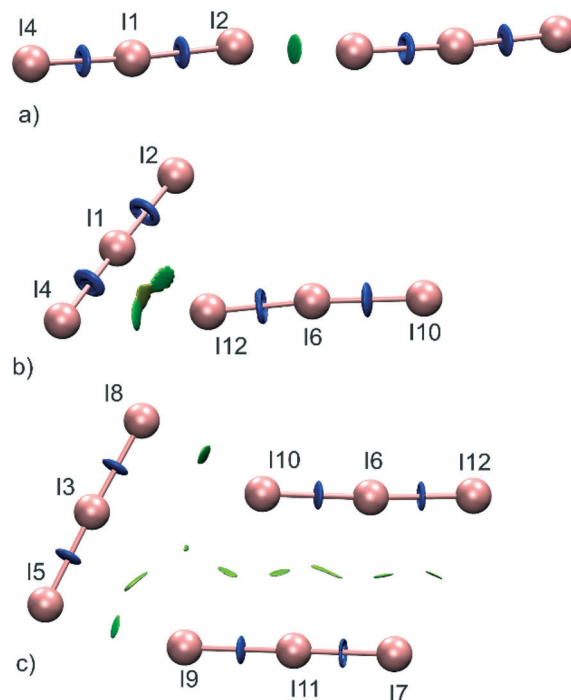van der Waals interactions combine three [I_3] units, shown in Fig. 11c, into a 2D network. These fragments are not fully planar; however, they do mostly reside in the *ab* plane. Therefore, this picture correlates well with the band structure, which shows that charge carriers are mostly mobile along the *b* direction and in the *ab* plane. Thus, we can describe the iodine sublattice as a 2D network based on the NCI interactions of varying strengths.

The black color of compounds **2** and **3** corresponds well to the results of the optical diffuse reflectance spectroscopy. Extrapolation of the linear part of the Kubelka–Munk plot[46] onto the energy axis gives a value of 1.37 eV for both compounds in the direct band gap approximation (ESI,† Fig. S8). Notably, the latter resembles the band gap in crystalline iodine (1.3 eV), which shows that the non-covalent interactions facilitate and support the arrangements of structural units into a motif that has electron transport properties similar to those of crystalline iodine. Therefore, the contribution of these interactions to the properties of the compound is essential and at least as important as that of the covalent contacts.

Experimental

5,7-Dimethyl-1,3-diazaadamantane-6-one

Urotropine (56.00 g, 400 mmol) was dissolved in a mixture of 200 mL of *n*-butanol and 45 mL of acetic acid, and pentanone-3 (42.80 mL, 400 mmol) was added. The reaction mixture was refluxed for 3 h. All volatiles were removed on a

rotary evaporator, and the resulting red oil was extracted 6 times with 220 mL of hot heptane. The extract was purified by hot filtration through basic alumina and evaporated. The orange powder was dissolved in 223 mL of DCM and washed twice with 22 mL of water. The organic layer was separated, dried over sodium sulfate, and evaporated to dryness. The yield of pink powder was 48.27 g (67%).

^{1}H-NMR (400 MHz, δ, ppm, CDCl$_3$) 0.89 (6H, s, CH$_3$), 3.04 (4H, d,^3J = 12.59 Hz, CH$_2$), 3.27 (4H, d,^3J = 12.59 Hz, CH$_2$), 4.13 (2H, s, CH$_2$). The ^{1}H-NMR spectrum is consistent with the literature data.[47]

5,7-Dimethyl-1,3-diazaadamantane

5,7-Dimethyl-1,3-diazaadamantane-6-one (1.80 g, 10 mmol) was dissolved in a mixture of hydrazine hydrate (15.12 mL), sodium hydroxide (1.51 g, 38 mmol) and ethylene glycol (7.6 mL) upon heating. The reaction mixture was refluxed for 16 h. All volatiles were distilled from the reaction mixture upon heating to 135 °C. The distillate was extracted with petroleum ether (75 mL), dried over sodium sulfate, and evaporated to dryness. The yield of white powder was 0.89 g (53%).

^{1}H-NMR (400 MHz, δ, ppm, CDCl$_3$) 0.63 (6H, s, CH$_3$), 1.48 (2H, s, CH$_2$), 2.78 (4H, d,^3J = 12.47 Hz, CH$_2$), 2.93 (4H, d,^3J = 12.35 Hz, CH$_2$), 3.96 (2H, s, CH$_2$). The ^{1}H-NMR spectrum is consistent with the literature data.[48]

Compounds 1–3

The synthesis of compounds **1–3** was performed using a solution of hydroiodic acid (stabilized), which was prepared by hydrolysis of freshly synthesized PI$_3$; details of this procedure can be found elsewhere.[49] The HI acid (stabilized) was distilled at 126 °C, and the resulting solution was diluted with distilled water to the required concentrations.

[(C$_{10}$N$_2$H$_{20}$)I]I (**1**) was prepared by dissolving 0.1 g of 5,7-dimethyl-1,3-diazaadamantane in 2 mL of 50% HI. After 48 hours, yellowish-white plate crystals were isolated from the solution. Compound **1** is stable in humid air over weeks.

[(C$_{10}$N$_2$H$_{20}$)I]I$_3$ (**2**) was synthesized in a solution prepared from 2 mL of H$_2$O, 0.2 mL of HI (50 wt%), and I$_2$ (0.1530 g). 5,7-Dimethyl-1,3-diazaadamantane (0.1 g) was added to the solution, which was then maintained under parafilm for 96 hours. Brown needle crystals were separated by filtration under vacuum and dried at room temperature. Compound **2** is stable in open air over several weeks.

[(C$_{10}$N$_2$H$_{20}$)(H$_2$O)](I$_3$)$_2$ (**3**) was obtained in the same way as **2** but by increasing the amount of iodine twice. The resulting solid formed as grey needle-like crystals with a yellowish luster. Compound **3** is stable in air at 4–6 °C for several months; at room temperature, discoloration of the solid is observed within several days.

Thermal analysis

Thermogravimetric analysis was performed using a NETZSCH 209 F1 Libra thermobalance. Samples were heated in alumina crucibles under dry nitrogen flow up to 673 K with a heating rate of 5 or 10 K min^{-1}. The NETZSCH Proteus Thermal Analysis program was used for the data processing.

Powder X-ray diffraction analysis (PXRD)

Was performed on an Imaging Plate Guinier Camera (Huber G670, Cu-K$_{\alpha1}$ radiation, λ = 1.540598 Å). The data were collected by scanning the image plate 4 times upon an exposure time of 1200 s at room temperature in the 2θ range of 3–100 deg. For the data collection, crystals were finely crushed in an agate mortar, and the resulting powder was fixed on a holder using Scotch tape.

Crystal structure determination

Well-shaped single crystals of **1** and **3** were selected from the respective synthetic samples. The single crystal diffraction data were measured at 100(2) K on a Bruker D8 VENTURE with a PHOTON 100 CMOS detector system equipped with a Mo-target X-ray tube (0.71073 Å). A frame width of 0.50° and an exposure time of 15 s per frame were employed for data collection. Data reduction and integration were performed with the Bruker software package SAINT (version 8.38A).[50] Data were corrected for absorption effects using the semi-empirical methods (multi-scan) as implemented in SADABS (version 2018/2)[51] for **1** and numerical methods for **3**. The crystal structures were solved by the intrinsic phase methods using the SHELXT (version 2018/2) program package,[52] which gave the positions of the iodine atoms. The positions of the nitrogen and carbon atoms were found from successive difference Fourier syntheses. The crystal structures were refined in anisotropic approximations of atomic displacement parameters for all the atoms except the hydrogens. The hydrogen atoms of the cations were calculated and further refined using riding models for both structures. Three of four hydrogen atom positions in two H$_2$O molecules for **3** were found from difference Fourier syntheses, and the position of the last hydrogen atom was calculated from geometric considerations. All four hydrogen atomic positions were refined freely with their isotropic atomic displacement parameters restricted to 1.5 times of their parent oxygen atom equivalent isotropic displacement parameter. The H–O bond distances were restrained to 0.82 Å with an estimated standard deviation of 0.02 Å.

The X-ray diffraction data for single crystals of **2** were collected at 293 K using a STOE STADI VARY diffractometer equipped with a Pilatus 100 K detector using a rotation method, a collimating mirror, and Mo Kα (0.71073 Å) radiation. STOE X-AREA software was used for the cell refinement and data reduction. Data collection and image processing were performed with X-Area 1.67 (STOE&Cie GmbH, Darmstadt, Germany, 2013). The intensity data were scaled up with LANA (part of X-Area) to minimize the differences in the intensities of the symmetry-equivalent reflections (multi-scan method). The structures were solved and refined with the SHELX program.[52] The non-hydrogen atoms were refined using the anisotropic full

matrix least-squares procedure. The hydrogen atoms of the cations were calculated and further refined using the riding models. Low intensity of the collected reflections led to low fractions of the reflections used in the refinement. Because all the checked crystals showed the same problem, the crystal structures were additionally confirmed by Rietveld refinement of X-ray powder diffraction data using Jana2006 programs.[53] For more details, see the ESI,† Fig. S3 and Table S3.

A summary of the experimental and crystallographic information for compounds **1–3** is given in Table 3. Selected interatomic distances and hydrogen bonds are shown in Tables 1 and 2, respectively. Full lists of interatomic distances within cations are placed in the ESI† (Table S2).

CCDC 2022254, 2022255, and 2022256 (single crystals of compounds **1**, **3**, and **2**, respectively) and 2034417 (powder, compound **2**) contain the supplementary crystallographic data for this paper.

Raman spectroscopy

Raman spectra of compounds **2** and **3** were recorded on a Renishaw In *via* spectrometer with a laser wavelength of $\lambda = 514$ nm (Ar, 50 mW). Sample investigations were performed in the backscattering geometry using a Leica DMLM confocal microscope (100′ lens) at room temperature in air. The focus distance was 250 mm, and the size of the laser beam was 20 μm. A CCD-camera (1024 × 368 pixels) was used as a detector. The scale was calibrated using monocrystalline silica (521.5 cm^{-1}) as a standard sample. WiRE 3.4 software was used for data processing.

Optical spectroscopy

Optical diffuse reflectance spectra were recorded using a UV-vis spectrometer (Perkin-Elmer Lambda 950, Perkin-Elmer, Waltham, MA, US) with an attached diffuse reflectance accessory. Measurements were performed at 298 K in the spectral range of 250–1200 nm with a scanning rate of 2 nm s^{-1} using finely ground polycrystalline samples. The data were transformed into absorbances using the Kubelka–Munk method and plotted as $[(k/s) \cdot h\nu]^2$ against $h\nu$, where k is the absorption coefficient, s is the scattering coefficient, and h is the Planck constant. The optical band gap, E_g, was approximated by extrapolation to $k = 0$.

Electronic structure calculations and bonding analysis

DFT calculations on the 3D structure of **3** were performed using the projector augmented wave method (PAW) as implemented in the Vienna *Ab initio* simulation package (VASP).[54,55] The Perdew–Burke–Ernzerhof exchange–correlation functional (PBE)[56] of the GGA type was used for the calculations, with a Brillouin zone sampling employing a Monkhorst-Pack[57] grid of 10 × 8 × 4 k-points. The PBE exchange–correlation functional has been proved to be a robust choice for periodic calculations on similar systems; for instance, see a recent paper by Hu *et al.* on copper polyiodides.[58] The energy cutoff was set to 450 eV, and the

Table 3 Data collection and structure refinement parameters for compounds **1–3**

Parameters	$[(C_{10}N_2H_{20})I]I$ (**1**)	$[(C_{10}N_2H_{20})I]I_3$ (**2**)	$[(C_{10}N_2H_{20})(H_2O)](I_3)_2$ (**3**)
Crystal system	Orthorhombic	Triclinic	Monoclinic
Space group	$Pbca$ (no. 61)	$P\bar{1}$ (no. 2)	$P2_1/n$ (no. 14)
a, Å	13.3082(8)	8.1345(12)	15.2610(19)
b, Å	11.9672(8)	8.6866(16)	9.3873(12)
c, Å	17.9425(11)	13.0650(10)	31.291(4)
α,°	90	95.775(9)	90
β,°	90	98.828(10)	101.966(2)
γ,°	90	96.093(10)	90
V, Å^3	2857.6(3)	900.7(2)	4385.3(10)
Z	8	2	8
d_{calc}	1.962	2.492	2.871
Diffractometer	Bruker D8 venture PHOTON 100 CMOS	IPDS Stoe Pilatus100 K	Bruker D8 venture PHOTON 100 CMOS
Radiation/wavelength	MoKα/0.71073	MoKα/0.71073	MoKα/0.71073
Temperature, K	100(2)	293(2)	100(2)
Crystal form	Plate	Needle	Needle
Crystal size, mm	0.03 × 0.09 × 0.18	0.01 × 0.01 × 0.10	0.018 × 0.09 × 0.189
Absorption correction	Multi-scan	Multi-scan	Numerical
θ range (data collection)	3.061–32.090	1.589–28.745	2.755–28.731
Range of h, k, l	$-19 \rightarrow h \rightarrow 19$; $-17 \rightarrow k \rightarrow 17$; $-26 \rightarrow l \rightarrow 26$	$-10 \rightarrow h \rightarrow 10$; $-11 \rightarrow k \rightarrow 11$; $-17 \rightarrow l \rightarrow 17$	$-20 \rightarrow h \rightarrow 20$; $-12 \rightarrow k \rightarrow 12$; $-42 \rightarrow l \rightarrow 42$
R_{int}	0.0581	0.142	0.0773
R/R_w	0.0314/0.0415	0.0527/0.1616	0.0579/0.0887
GoF	1.118	0.664	1.178
No. of params./reflections	130/4984	147/4133	358/11337
$\Delta\rho_{max}$ (e/Å^{-3}) positive/negative	0.65/−0.68	0.83/−0.87	1.765/−1.969

energy convergence criterion was 10^{-5} eV. Convergence towards the k-point set and energy was checked. DFT calculations on the iodine fragments were performed using the hybrid B3LYP[59] functional, which is standard for molecular system studies, and the def2-QZVPPD basis set[60] (28 e^- core ECP28MDF)[61] utilizing the Orca 4.2.0 package.[62,63] In both types of calculations, the DFT-D3 dispersion correction by Grimme was used.[64] Chemical bonding analysis was performed *via* studying the QTAIM charge density (3D structure), electron localizability indicator (ELI-D, molecular calculations)[65] and RDG (non-covalent interactions, NCI, molecular calculations)[66] topology. Topological analyses of the charge density and ELI-D were performed using the DGrid 4.6 package,[67] and NCI analysis was performed using the Multiwfn 3.7 package.[68] ELI-D was visualized using the VESTA 3 package,[69] and NCI plots were obtained using VMD 1.9.3.[70]

Conclusions

We have shown that under highly acidic conditions, 5,7-dimethyl-1,3-diazaadamantane can be doubly protonated, giving rise to the supramolecular building blocks $[(C_{10}N_2H_{20})I]^+$ and $[(C_{10}N_2H_{20})(H_2O)]^{2+}$. Depending on the slightly varying synthetic conditions, these blocks are involved in the formation of the supramolecular architectures $[(C_{10}N_2H_{20})I]I$ (**1**), $[(C_{10}N_2H_{20})I]I_3$ (**2**), and $[(C_{10}N_2H_{20})(H_2O)](I_3)_2$ (**3**), in which the anionic inorganic part is composed purely of iodines. Those architectures feature a number of non-covalent interactions both within the cationic and anionic parts as well as between the cations and anions, which include remarkably short (N)H⋯I, (O)H⋯I, and (N)H⋯O hydrogen bonds as well as I⋯I interactions in the anionic substructure of $[(C_{10}N_2H_{20})(H_2O)](I_3)_2$ (**3**). The latter structure features a strand-shaped anionic substructure in which I_3^- anions are linked together by intermolecular forces of different strengths, ranging from secondary I⋯I interactions of 3.57–3.59 Å to weak I⋯I interactions at distances above 3.9 Å.

The analysis of the electronic structure of compound **3** allows one to evaluate regions with covalent and strong non-covalent interactions (halogen bonds) as well as regions with weak interactions related to dispersive forces; however, the band structure confirms that even weak interactions contribute to the enhanced mobility of charge carriers. Also, these new materials are highly prominent for their stability in strong acidic media; as such, they can serve as precursors for the conversion of metallic lead into perovskite-like iodoplumbates, which are used as light-harvesting materials in solar cells.

Author contributions

All authors have given approval to the final version of the manuscript.

Conflicts of interest

There are no conflicts to declare.

Notes and references

1 P. H. Svensson and L. Kloo, *Chem. Rev.*, 2003, **103**, 1649–1684.
2 A. Hagfeldt, G. Boschloo, L. Sun, L. Kloo and H. Pettersson, *Chem. Rev.*, 2010, **110**, 6595–6663.
3 M. Grätzel, *Inorg. Chem.*, 2005, **44**, 6841–6851.
4 I. Turkevych, S. Kazaoui, N. A. Belich, A. Y. Grishko, S. A. Fateev, A. A. Petrov, T. Urano, S. Aramaki, S. Kosar, M. Kondo, E. A. Goodilin, M. Grätzel and A. B. Tarasov, *Nat. Nanotechnol.*, 2019, **14**, 57–63.
5 A. A. Petrov, N. A. Belich, A. Y. Grishko, N. M. Stepanov, S. G. Dorofeev, E. G. Maksimov, A. V. Shevelkov, S. M. Zakeeruddin, M. Grätzel, A. B. Tarasov and E. A. Goodilin, *Mater. Horiz.*, 2017, **4**, 625–632.
6 N. A. Belich, A. A. Petrov, P. O. Rudnev, N. M. Stepanov, I. Turkevych, E. A. Goodilin and A. B. Tarasov, *ACS Appl. Mater. Interfaces*, 2020, **12**, 20456–20461.
7 T. A. Shestimerova and A. V. Shevelkov, *Russ. Chem. Rev.*, 2018, **87**, 28–48.
8 E. V. Bartashevich and V. G. Tsirelson, *Russ. Chem. Rev.*, 2014, **83**, 1181–1203.
9 J. Rusnik, S. Swen-Walstra and T. Migchelsen, *Acta Crystallogr., Sect. B: Struct. Crystallogr. Cryst. Chem.*, 1972, **28**, 1331–1335.
10 E. V. Savinkina, B. N. Mavrin, D. V. Albov, V. V. Kravchenko and M. G. Zaitseva, *Russ. J. Coord. Chem.*, 2009, **35**, 96–100.
11 T. A. Shestimerova, M. A. Bykov, Z. Wei, E. V. Dikarev and A. V. Shevelkov, *Russ. Chem. Bull.*, 2019, **68**, 1520–1524.
12 T. A. Shestimerova, N. A. Yelavik, A. V. Mironov, A. N. Kuznetsov, M. A. Bykov, A. V. Grigorieva, V. V. Utochnikova, L. S. Lepnev and A. V. Shevelkov, *Inorg. Chem.*, 2018, **57**, 4077–4087.
13 T. A. Shestimerova, N. A. Golubev, N. A. Yelavik, M. A. Bykov, A. V. Grigorieva, Z. Wei, E. V. Dikarev and A. V. Shevelkov, *Cryst. Growth Des.*, 2018, **18**, 2572–2578.
14 S. A. Adonin, A. N. Usoltsev, A. S. Novikov, B. A. Kolesov, V. P. Fedin and M. N. Sokolov, *Inorg. Chem.*, 2020, **59**, 3290–3296.

15   S. A. Adonin, A. S. Novikov and M. N. Sokolov, *Eur. J. Inorg. Chem.*, 2019, 4221–4223.

16   A. Starkholm, L. Kloo and P. H. Svensson, *ACS Appl. Energy Mater.*, 2019, **2**, 477–485.

17   G. J. Reiß and J. S. Engel, *CrystEngComm*, 2002, **4**, 155–161.

18   O. I. Bol'shakov, I. D. Yushina, E. V. Bartashevich, Y. V. Nelyubina, R. R. Aysin and O. A. Rakitin, *Struct. Chem.*, 2017, **28**(6), 1927–1934.

19   A. Abate, M. Brischetto, G. Cavallo, M. Lahtinen, P. Metrangolo, T. Pilati, S. Radice, G. Resnati, K. Rissanen and G. Terraneo, *Chem. Commun.*, 2010, **46**, 2724–2726.

20   A. N. Usoltsev, A. S. Novikov, B. A. Kolesov, K. V. Chernova, P. E. Plyusnin, V. P. Fedin, M. N. Sokolov and S. A. Adonin, *J. Mol. Struct.*, 2020, **1209**, 127949.

21   I. D. Yushina, N. M. Tarasova, D. G. Kim, V. V. Sharutin and E. V. Bartashevich, *Crystals*, 2019, **9**, 506–519.

22   E. V. Bartashevich, S. E. Mukhitdinova, I. D. Yushina and V. G. Tsirelson, *Acta Crystallogr., Sect. B: Struct. Sci., Cryst. Eng. Mater.*, 2019, **75**, 117–126.

23   A. Peuronen, H. Rinta and M. Lahtinen, *CrystEngComm*, 2015, **17**, 1736–1740.

24   J. Zhang, S. Han, C. Ji, W. Zhang, Y. Wang, K. Tao, Z. Sun and J. Luo, *Chem. – Eur. J.*, 2017, **23**, 17304–17310.

25   T. Li, Y. Hu, C. A. Morrison, W. Wu, H. Hana and N. Robertson, *Sustainable Energy Fuels*, 2017, **1**, 308–316.

26   M. Węcławik, P. Szklarz, W. Medycki, R. Janicki, A. Piecha-Bisiorek, P. Zieliński and R. Jakubas, *Dalton Trans.*, 2015, **44**, 18447–18458.

27   T. Sun, F. Liang, X. Zhang, H. Tu, Z. Lin, G. Zhang and Y. Wu, *Polyhedron*, 2017, **127**, 478–488.

28   H. Cui, R. Goddard and K.-R. Porschke, *J. Phys. Org. Chem.*, 2012, **25**, 814–827.

29   K.-F. Tebbe and K. Nagel, *Z. Anorg. Allg. Chem.*, 1995, **621**, 225–228.

30   N. S. Zefirov, V. A. Palyulin, O. I. Levina, K. A. Potekhin, E. N. Kurkutova and Y. T. Struchkov, *Vestn. Mosk. Univ., Ser. 2: Khim.*, 1987, **28**, 276.

31   B.-G. Chen, *J. Cluster Sci.*, 2017, **28**, 983–994.

32   J.-H. Lee, N. C. Bristowe, P. D. Bristowe and A. K. Cheetham, *Chem. Commun.*, 2015, **51**, 6434–6437.

33   S. Alvarez, *Dalton Trans.*, 2013, **42**, 8617–8636.

34   I. Yu. Chernyshov, I. V. Ananyev and E. A. Pidko, *ChemPhysChem*, 2020, **21**, 370–376.

35   N. Yamanaka, R. Kawano, W. Kubo, N. Masaki, T. Kitamura, Y. Wada, M. Watanabe and S. Yanagida, *J. Phys. Chem. B*, 2007, **111**, 4763–4769.

36   I. D. Yushina, V. I. Batalov, E. V. Bartashevich, A. O. Davydov, P. S. Zelenovskiy and A. Masunov, *J. Raman Spectrosc.*, 2017, **48**, 1411–1413.

37   P. Deplano, J. R. Ferraro, M. L. Mercuri and E. F. Trogu, *Coord. Chem. Rev.*, 1999, **188**, 71–95.

38   S. Saha, H. Okajima, O. Homma and H. Hamaguchi, *Spectrochim. Acta, Part A*, 2017, **176**, 79–82.

39   P. H. Svensson and L. Kloo, *J. Chem. Soc., Dalton Trans.*, 2000, 2449–2455.

40   L. Kloo, J. Rosdahl and P. H. Svensson, *Eur. J. Inorg. Chem.*, 2002, 1203–1209.

41   J. M. Williams, H. H. Wang, T. J. Emge, U. Geiser, M. A. Beno, P. C. W. Leung, K. D. Carlson, R. J. Thorn and A. J. Schultz, *Prog. Inorg. Chem.*, 1987, **35**, 51–218.

42   P. Pyykko, *Chem. Rev.*, 1997, **97**, 597–636.

43   G. A. Landrun, N. Goldberg and R. Hoffmann, *J. Chem. Soc., Dalton Trans.*, 1997, 3605–3613.

44   E. R. Johnson, S. Keinan, P. Mori-Sánchez, J. Contreras-García, A. J. Cohen and W. Yang, *J. Am. Chem. Soc.*, 2010, **132**(18), 6498–6506.

45   R. A. Boto, J. Contreras-Garcia, J. Tierny and J.-P. Piquemal, *Mol. Phys.*, 2015, **114**, 1406–1414.

46   P. Kubelka and F. Munk, *Z. Tech. Phys.*, 1931, **12**, 593–601.

47   A. V. Medved'ko, B. V. Egorova, A. A. Komarova, R. D. Rakhimov, D. P. Krut'ko, S. N. Kalmykov and S. Z. Vatsadze, *ACS Omega*, 2016, **1**(5), 854–867.

48   P. Comba, L. Daumann, J. Lefebvre, G. Linti, B. Martin, J. Straub and T. Zessin, *Aust. J. Chem.*, 2009, **62**(10), 1238–1245.

49   N. A. Yelovik, A. V. Mironov, M. A. Bykov, A. N. Kuznetsov, A. V. Grigorieva, Z. Wei, E. V. Dikarev and A. V. Shevelkov, *Inorg. Chem.*, 2016, **55**, 4132–4140.

50   SAINT, Version 8.38A; Bruker AXS Inc.: Madison, WI, USA, 2019.

51   L. Krause, R. Herbst-Irmer, G. M. Sheldrick and D. Stalke, *J. Appl. Crystallogr.*, 2015, **48**, 3–10.

52   G. M. Sheldrick, SHELXT–Integrated space-group and crystal-structure determination, *Acta Crystallogr., Sect. C: Struct. Chem.*, 2015, **71**, 3–8.

53   V. Petricek, M. Dusek and L. Palatinus, *Z. Kristallogr. – Cryst. Mater.*, 2014, **229**, 345–352.

54   G. Kresse and D. Joubert, *Phys. Rev. B*, 1999, **59**, 1758–1775.

55   G. Kresse and J. Furthmüller, Vienna Ab initio simulation package (VASP), v.5.3, http://www.vasp.at/.

56   J. P. Perdew, K. Burke and M. Ernzerhof, *Phys. Rev. Lett.*, 1996, **77**, 3865.

57   H. J. Monkhorst and J. D. Pack, *Phys. Rev. B*, 1976, **13**, 5188–5192.

58   J. Hu, J. Zhou and S. Cao, *Dalton Trans.*, 2018, **47**, 17216–17220.

59   A. D. Becke, *J. Chem. Phys.*, 1993, **98**, 5648.

60   D. Rappoport and F. Furche, *J. Chem. Phys.*, 2010, **133**, 134105.

61   B. Metz, H. Stoll and M. Dolg, *J. Chem. Phys.*, 2000, **113**, 2563–2569.

62   F. Neese, *Wiley Interdiscip. Rev.: Comput. Mol. Sci.*, 2012, **2**, 73.

63   F. Neese, *Wiley Interdiscip. Rev.: Comput. Mol. Sci.*, 2017, **8**, e1327.

64   S. Grimme, J. Antony, S. Ehrlich and H. Krieg, *J. Chem. Phys.*, 2010, **132**, 154104.

65   M. Kohout, K. Pernal, F. R. Wagner and Y. Grin, *Theor. Chem. Acc.*, 2004, **112**, 453–459.

66   E. R. Johnson, S. Keinan, P. Mori-Sánchez, J. Contreras-García, A. J. Cohen and W. Yang, *J. Am. Chem. Soc.*, 2010, **132**, 6498–6506.

67 M. Kohout, DGrid, ver. 5.1; Radebeul, 2019, http://www2.cpfs.mpg.de/~kohout/dgrid.html.

68 T. Lu and F. Chen, *J. Comput. Chem.*, 2012, **33**, 580–592.

69 K. Momma and F. Izumi, *J. Appl. Crystallogr.*, 2011, **44**, 1272–1276.

70 W. Humphrey, A. Dalke and K. Schulten, *J. Mol. Graphics*, 1996, **14**, 33–38.